

# Empirical mode decomposition and Hilbert transforms for analysis of oil-film interferograms

Kapil Chauhan, Henry C H Ng and Ivan Marusic

Department of Mechanical Engineering, The University of Melbourne, Victoria 3010, Australia

E-mail: [kchauhan@unimelb.edu.au](mailto:kchauhan@unimelb.edu.au), [h.ng4@pgrad.unimelb.edu.au](mailto:h.ng4@pgrad.unimelb.edu.au) and [imarusic@unimelb.edu.au](mailto:imarusic@unimelb.edu.au)

Received 13 March 2010, in final form 9 July 2010

Published 25 August 2010

Online at [stacks.iop.org/MST/21/105405](http://stacks.iop.org/MST/21/105405)

## Abstract

Oil-film interferometry is rapidly becoming the preferred method for direct measurement of wall shear stress in studies of wall-bounded turbulent flows. Although being widely accepted as the most accurate technique, it does have inherent measurement uncertainties, one of which is associated with determining the fringe spacing. This is the focus of this paper. Conventional analysis methods involve a certain level of user input and thus some subjectivity. In this paper, we consider empirical mode decomposition (EMD) and the Hilbert transform as an alternative tool for analyzing oil-film interferograms. In contrast to the commonly used Fourier-based techniques, this new method is less subjective and, as it is based on the Hilbert transform, is superior for treating amplitude and frequency modulated data. This makes it particularly robust to wide differences in the quality of interferograms.

**Keywords:** oil-film interferometry, Hilbert–Huang transforms, empirical mode decomposition

## 1. Introduction

Wall shear stress,  $\tau_w$ , in wall-bounded flows is an important quantity that needs to be measured in studies of drag characteristics, scaling of mean flow and other turbulence statistics. The measurement of  $\tau_w$  has been the focus of many studies [1–5] and in recent years oil-film interferometry has emerged as a preferred technique. The oil-film interferometer provides a direct measure of the wall shear stress, as opposed to the classical methods such as the Clauser chart [6, 7] and the Preston tube [8, 9], which require *a priori* assumption of known universal scaling laws. However, the analytical methods used to extract the fringe spacing and hence the wall shear stress,  $\tau_w$ , from the oil-film interferograms introduce a certain degree of user subjectivity. Common approaches that exist for the extraction of the fringe spacing are the  $x-t$  diagram, maximum entropy spectral techniques and correlation-based methods. Details of the approaches for various applications are available in numerous recent works [1–4, 10–12]. Ideally, when it is assumed that the average wall shear stress is constant, a line taken perpendicular to the fringe pattern will yield a sinusoid with constant amplitude and wavenumber, where maxima and minima will correspond to the center of the light

and dark bands of the interference pattern, respectively. The fringe spacing could then easily be determined by finding the dominant wavenumber using Fourier spectral methods. However, when dealing with real interferograms the data are rarely globally both linear and stationary. This makes accurate identification of the dominant wavenumber difficult because any globally non-uniform wavenumbers will cause energy spreading and spurious harmonics to appear in the Fourier energy spectrum. Most oil-film interferometry techniques require a user-chosen line or region that is analyzed. Region selection is also required because the oil-film interferograms are sensitive to contamination, mainly due to dust, bubbles in the oil or other contaminants. The process of selecting the interrogation window can be problematic because there is no systematic method and one relies on visual inspection of the interferograms. In cases of highly contaminated oil films, the entire sequence of interferograms might have to be discarded.

Here an alternative method is introduced for the extraction of the fringe spacing from oil-film interferograms. This method largely overcomes the limitations associated with the Fourier transform as well as providing a method to estimate the fringe spacing from contaminated interferograms. A relatively new technique, the empirical mode decomposition

(EMD) [13], coupled with the Hilbert transform allows one to overcome the limitations of Fourier spectral methods and can be used to analyze non-stationary and nonlinear data series. The method involves two steps: first, EMD is applied to the data series to obtain a set of intrinsic mode functions (IMFs), which are symmetrical about the mean and based on the intrinsic characteristic scales of the data itself. In the second step, the Hilbert transform is applied to the IMFs to generate the time–wavenumber–energy distribution of the data. The EMD and Hilbert transform technique developed by Huang *et al* [13] was originally used in the study of nonlinear water waves [14] and is also referred to as the Hilbert–Huang transform (HHT). The technique is adapted here for the extraction of fringe spacing from oil-film interferograms and overcomes largely the need to preselect the region of interrogation, avoiding edge and three-dimensional effects.

## 2. Oil-film interferometry

The oil-film interferometer measures wall shear stress,  $\tau_w$ , by determining the thinning rate of an oil film that is placed on the bounding surface of the flow regime of interest. This method of measuring the skin friction has been applied to the study of canonical turbulent boundary layers, flows over aerofoils and flows over turbine blades. The seminal work of Tanner and Blows [15] established the relationship between the wall shear stress and the thinning rate of the oil film, which is governed by the thin oil-film equation of Squire [16]. Tanner [17, 18] and Tanner and Kulkarni [19] continued to develop the technique and further work by Monson [20], and Monson and Higuchi [21] modified and further improved the oil-film interferometer. There are many variations of the oil-film interferometry technique, and these fall into the categories of point, line and image-based techniques. Designations include the laser interferometer skin friction (LISF), fringe imaging skin friction (FISF), global imaging skin friction (GISF) and surface imaging skin friction (SISF) methods. A comprehensive review of the various methods is given by Naughton and Sheplak [3]. Over the course of time, the technique has continued to evolve given the advances in image acquisition technology and improvements to the analysis techniques.

Oil-film interferometry is based on the relationship between the thinning rate of the oil film and the three forces that may act upon it: gravity, pressure and shear force. When the oil film is sufficiently thin, the effect of gravity and pressure forces becomes negligible and the thinning rate of the oil film is assumed to be linear. A simple relationship then exists between the thinning rate of the oil and the shear force acting upon it. When a coordinate system is defined such that  $x$  is the streamwise direction,  $y$  is the wall normal direction and  $z$  is the spanwise direction, one can obtain the wall shear stress as

$$\tau_w = \frac{2\mu_{\text{oil}}\sqrt{n_{\text{oil}}^2 - n_{\text{air}}^2} \sin^2 \theta}{\lambda} \frac{\Delta x}{\Delta t}, \quad (1)$$

where  $\tau_w$  is the wall shear stress,  $\lambda$  is the wavelength of the light source,  $\mu_{\text{oil}}$  is the viscosity of the oil,  $n_{\text{oil}}$  and  $n_{\text{air}}$  are

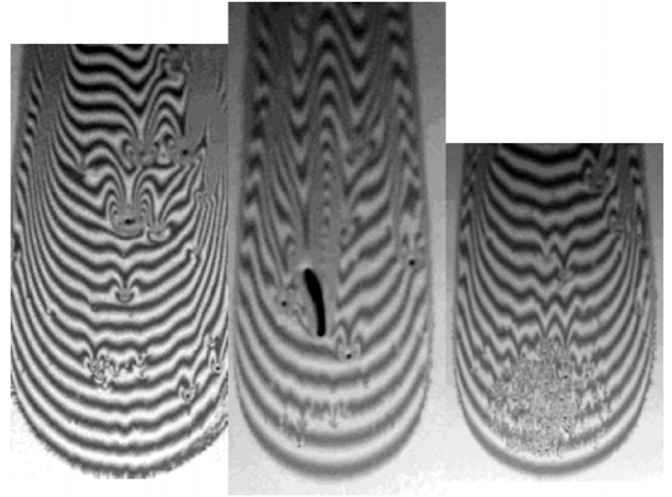


**Figure 1.** Examples of oil-film interferometry images from different experiments. Only typical examples of contaminated images are shown.

the refractive indices of the oil and air, respectively,  $\theta$  is the illumination incidence angle and  $\Delta x$  is the difference in the distance between consecutive fringes (relative to the leading edge of the oil film) [2, 11, 21, 22]. Equation (1) is applicable to flow where the thinning rate of the oil film can be assumed to be linear and change in shear stress is small over the distance that is being measured.

Figure 1 shows the evolution of oil drop as it is acted upon by shear from an air flow passing over it under different flow conditions. Initially, the droplet of oil is deformed by the force acting on it and over time the oil spreads and thins to form a film with thickness of the order of a few microns. The fringes are generated by Fizeau interferometry and the fringe spacing increases over time as the oil film becomes thinner. In almost all laboratory applications, the oil films are subject to contamination due to dust particles or air bubbles getting caught in the film and these disturbances can be seen in sample acquisitions shown in figure 1. If a line is taken through a contaminated region in the interferogram, the resulting signal of light intensity as a function of streamwise distance will feature discontinuities. These spurious peaks are caused by the dust particles that locally raise the oil film surface and hence are highly reflective. It is also apparent that the disturbances due to dust are not isolated and the flow around and behind them is also altered; i.e. there is an effect on the observed fringe spacing surrounding the disturbance. Since the wall shear stress is based on the time history of the fringe spacing, it is clear that the disturbances in the oil film pose a significant problem because they will propagate through the entire time history. This can lead to errors in the calculated value of skin friction and if the films are severely contaminated, the data must be discarded. Most analytical methods use some form of region or line selection in order to avoid errors caused by contamination of the oil films to propagate through the analysis. One of the aims of this paper is to provide a technique that will remove the subjectivity involved in selecting the interrogation region. The following sections outline the use of the empirical mode decomposition and the Hilbert transform

as a tool for the extraction of the fringe spacing in a method that does not require such user inputs.

### 3. Techniques for analysis of interferograms

As mentioned earlier, estimating the thinning of the oil film with time is an important requirement in accurate determination of  $\tau_w$ . This in turn requires calculating the fringe spacing (in physical space) and its change with time. For images that are acquired digitally this is easily done by processing the images to determine the distance between two consecutive fringes in terms of the pixels. A reference calibration image then can provide conversion of  $\Delta x$  in pixels to  $\Delta x$  in physical space. However, determining the fringe spacing is not straightforward as the quality of images can differ significantly as shown in figure 1. For the sample images shown, it is observed that the interference pattern is visible in all of them with a widely varying degree of clarity. Surface contamination and dust in all of the examples cause an irregular fringe pattern in the flow direction and are characterized with non-uniform curvature. For a set of images acquired for a particular flow, the presence of any dirt leads to the user needing to determine the ‘region of analysis’, and this region of analysis largely depends on the size of contamination, which is not a control parameter. Accordingly, the usual procedure involves windowing the data in order to

- avoid edge and three-dimensional effects introduced by droplet curvature,
- select the portion of the interferogram or signal that is locally linear and stationary and discard the rest in order to use Fourier methods, and
- maximize the signal-to-noise ratio of the experimental data.

Another feature to be noted is the varying features of fringes as they appear different under different lighting conditions and image acquisition setup. Thus, images with weak contrast might again be difficult to use if a good region of analysis is not visually identifiable. Typically, a set of images with such contamination would be discarded if it were to be analyzed by conventional techniques. As an example of one of the conventional approaches, a composite  $x-t$  diagram is shown in figure 2. This composite image is obtained by choosing a fixed array of pixels in the flow direction from multiple images acquired over time and then rearranging them to exhibit the location of a particular fringe at  $x$  in time. The fringe pattern in the composite image shows a linear relation between the fringe spacing and time. Hence, the slope of line drawn over the first fringe from the bottom is equivalent to  $\Delta x/\Delta t$ , while a similar line on the second fringe pattern will have a slope of  $2\Delta x/\Delta t$ . A user can draw many such lines on the  $x-t$  diagram and determine an average. However, a line can be drawn on either edge or the center of a fringe, which will result in different slope estimates. Also, one can only utilize a small region of the diagram (lower right) to visually identify fringe lines without ambiguity. Such an approach can introduce errors that depend on the user’s selection criteria and would not be consistent if the process is repeated. Hence, we

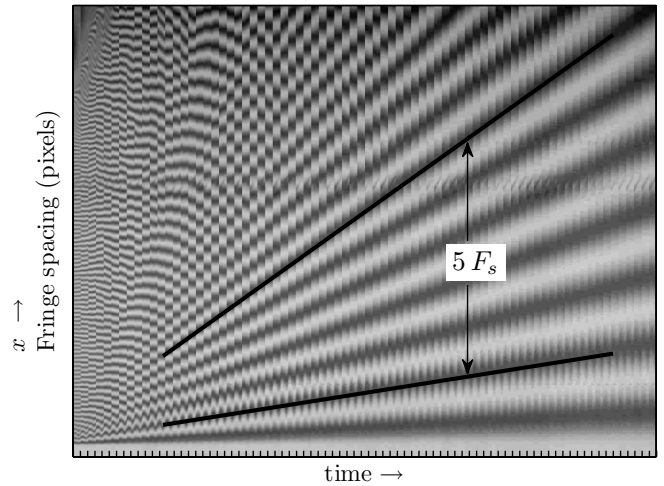


**Figure 2.** An  $x-t$  diagram or composite image showing development of the fringe pattern in time. The slope of the first dark band is  $\Delta x/\Delta t$ .

aim to use the HHT as a robust and statistical procedure that can extract the fringe spacing accurately even in the absence of ‘ideal’ fringe patterns throughout and with minimal user input.

The fast Fourier transform (FFT) is widely used in image processing and is also applied to oil-film interferograms to determine the fringe spacing. The Fourier transform  $\hat{f}(\omega)$  of an analytic function  $f(x)$  is given as

$$\hat{f}(\omega) = \frac{1}{2\pi} \int_{-\infty}^{\infty} f(x) e^{-i\omega x} dx. \quad (2)$$

An FFT of the intensity profile will result in a spectrogram which peaks at a wavenumber equivalent to the spacing between two dark and light bands in the fringe patterns. However, wavenumber determination by the FFT is only accurate for a linear and stationary signal. Its applicability also suffers from discontinuity, noise and signal length, which are typically present in intensity profiles as shown in figures 3, 5 and 6. As the signal in practical application is always finite, one can only calculate a discrete Fourier transform (DFT) by an FFT algorithm within a limited frequency/wavenumber range. The frequency range of a DFT depends on the sample size of the finite signal. This aspect will be discussed later in section 5.1.

The present study aims to improve on the techniques to extract fringe spacing by utilizing the HHT, which is a powerful tool in analysis of non-stationary data [13]. The Hilbert transform of an analytic function  $X(t)$  is given as

$$Y(t) = \text{P.V.} \frac{1}{\pi} \int_{-\infty}^{\infty} \frac{X(\tau)}{t - \tau} d\tau, \quad (3)$$

where P.V. indicates the Cauchy principal value. The Hilbert transform can be thought of as the convolution of  $X(t)$  with the function  $1/(\pi t)$ . An analytic signal  $Z(t)$  is obtained with

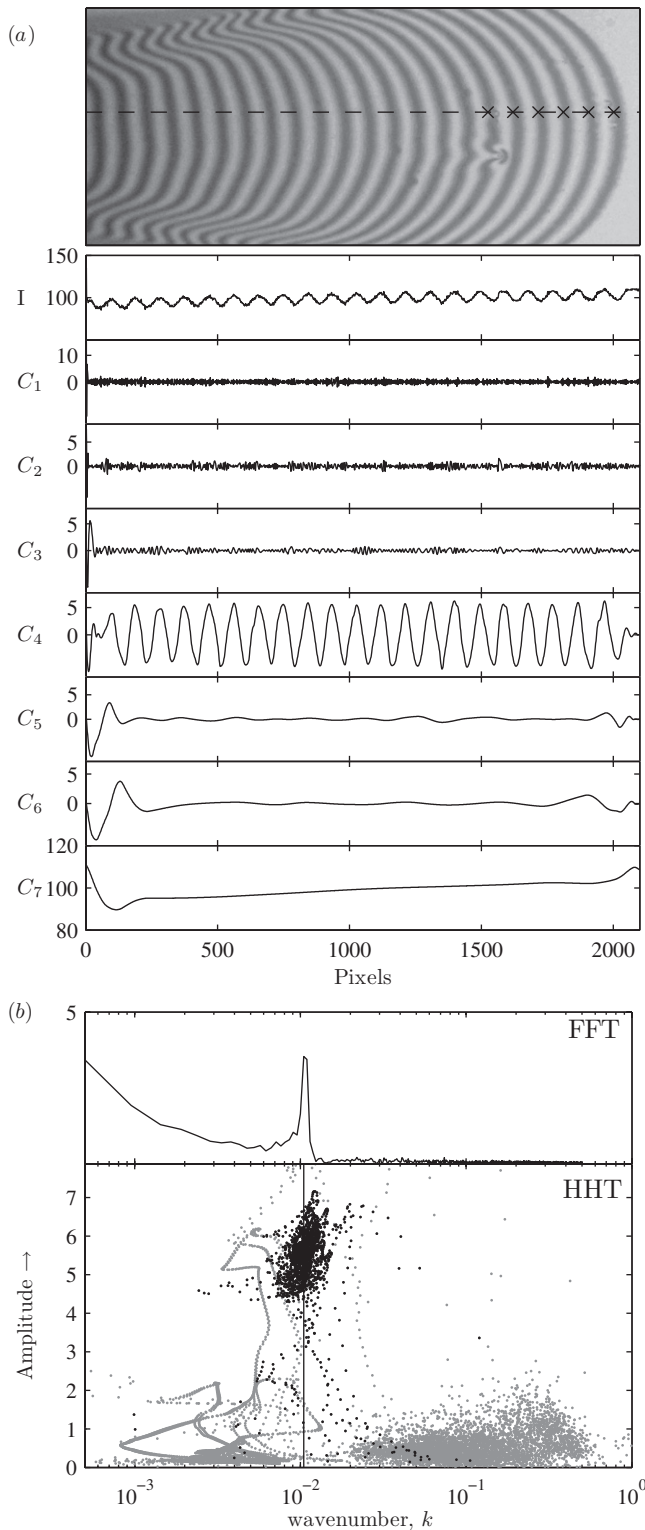


**Figure 3.** Example 1. (a) IMFs of the intensity profile at a pixel line shown by a dashed black line on the grayscale image on top.  $I$  is the intensity profile, and  $C_i$  are IMFs. (b) Amplitude versus wavenumber plots for the FFT and HHT. For the HHT, the wavenumber for mode containing fringe characteristics is shown in black and rest are in gray. A solid black line denotes the median of wavenumbers of the dominant mode.

$X(t)$  and  $Y(t)$  as a complex conjugate pair:

$$Z(t) = X(t) + iY(t) = \alpha(t) e^{i\theta(t)}, \quad (4)$$

in which

$$\alpha(t) = [X^2(t) + Y^2(t)]^{1/2}, \quad \theta(t) = \arctan\left(\frac{Y(t)}{X(t)}\right). \quad (5)$$

Here,  $\alpha$  is the amplitude and  $\theta$  is the phase angle. The polar coordinate representation can be thought of as the best local fit of an amplitude- and phase-varying trigonometric function to  $X(t)$ . A instantaneous frequency is then defined as

$$\omega(t) = \frac{d\theta(t)}{dt}. \quad (6)$$

A detailed discussion on instantaneous frequency and physical interpretation of Hilbert transform can be found in Huang *et al* [13] and Bendat and Piersol [23]. This definition of instantaneous frequency cannot be applied to any arbitrary signal. Physically, only one frequency exists at a particular instance in time and hence it can only represent one component of a signal. EMD proposed by Huang *et al* [13] decomposes the signal into ‘mono-component’ signals using certain criteria so that a relevant instantaneous frequency can be obtained for each of those decomposed functions. Hilbert transform applied to a signal in spatial domain would give the instantaneous wavenumber, as in the present case.

### 3.1. Empirical mode decomposition

The EMD technique is applied to decompose a data series into a set of intrinsic mode functions, or IMFs, so that the information of physical significance contained within the data can be obtained without distortion. Full details of these techniques are given in Huang *et al* [13, 14] and Bendat and Piersol [23]. By definition, IMFs must satisfy two conditions:

- (1) the total number of extrema and zero-crossings at most differ by one, and
- (2) the local mean defined by the envelope formed by the local maxima and the envelope formed by the local minima must be equal to zero.

A ‘sifting process’ (see [13]) is used to identify and separate the intrinsic modes of the signal,  $X(t)$ . Once identified, the maxima and minima are used to generate the upper and lower envelope functions of the data. The mean formed by the upper and lower envelopes,  $m_1$ , is then subtracted from the data to give  $h_1$ . The procedure of subtracting the mean of upper and lower envelopes is repeated on  $h_1$ :

$$X(t) - m_1 = h_1, \quad (7)$$

$$h_1 - m_{11} = h_{11}, \quad (8)$$

$$h_{11} - m_{12} = h_{12}, \quad (9)$$

$$\downarrow$$

$$h_{1(k-1)} - m_{1k} = h_{1k}. \quad (10)$$

If

$$SD = \frac{\sum (h_{1(k-1)} - h_{1k})^2}{\sum h_{1(k-1)}^2} < 0.2-0.3, \quad (11)$$

then  $C_1 = h_{1k}$  is an intrinsic mode. Once a function,  $C_1$ , that satisfies the IMF criteria is found, it becomes an IMF and is then subtracted from the original data series:

$$X(t) - C_1 = R_1.$$

The sifting procedure of equations (7)–(11) is repeated for  $R_1$  to find the next intrinsic mode,  $C_2$ . The entire process is then repeated until all IMFs are obtained. Essentially, the sifting process drives the mean of the envelopes formed by the local maxima and local minima to zero in order to satisfy the definition of an IMF. When all the IMFs are identified and removed from the data, there remains a residual function, which is generally the trend of the data series.

The sifting process requires a stop criterion; otherwise, the generated IMFs will be modes of constant amplitude and contain only frequency modulations. Without the amplitude modulation, the modes lose their physical meaning [13]. The stop criterion proposed by Huang *et al* [13] was to limit the standard deviation between consecutive sifts to values of between 0.2 and 0.3. Here, we impose the lower limit and an additional criterion based on the number of maxima or minima. If the number of maxima or minima falls below a certain threshold, the sifting process is stopped. In effect this implements a cutoff frequency to limit the number of IMFs generated and also to prevent the generation of spurious modes. The cutoff frequency will change for different applications but is generally a proportion of the lowest frequency occurring in the original data series. For the particular case of interferograms, if the image has high background noise a lower standard deviation is advised so that noise is limited to the first few modes. A larger value of standard deviation will inherently result in larger scatter in instantaneous frequencies. On the other hand, imposing a limit on the number of maxima/minima provides a means to limit higher trend containing modes being generated. Such modes contain low wavenumber features that are substantially lower than the characteristic wavenumber corresponding to the fringe spacing. Hence, increasing the standard deviation can lead to larger errors in determining dominant wavenumber/frequency of the characteristic IMF, while the number of maxima/minima determined during sifting only affects the computational time. The reader is referred to [13, 14] for details of the sifting process and EMD.

When analyzing an oil-film interferogram, the data series will consist of a line taken through an interferogram parallel to the flow direction. The signal obtained will contain multiple maxima and minima each corresponding to the light and dark bands that appear in the interferogram. When the EMD is applied to this signal, the time lapse between successive extremum of one of the obtained IMFs will be the fringe spacing of the oil-film interferogram. For oil-film interferograms, the cutoff wavenumber is a factor of the wavenumber that corresponds to the maximum fringe spacing within the entire time series. This can be determined by inspection of the last recorded interferogram.

#### 4. The experimental database

Measurements were performed on the floor of the high Reynolds number boundary layer wind tunnel (HRNBLWT) at the University of Melbourne. Following are the important features of the experiments that are relevant to results presented here.

- (a) Interferometry was performed at three different streamwise stations:  $x = 8$  m, 13 m and 21 m. The freestream velocity was also varied to obtain a range of Reynolds number,  $Re_x$  between  $6.7 \times 10^6$  and  $3.5 \times 10^7$ . Most measurements were repeated a number of times to check their repeatability and in case small problems occurred. Also, multiple oil droplets are used side by side to avoid repetition if a single oil film is contaminated.
- (b) The oil-film measurements were all performed on a glass plate mounted flush with the floor of the wind tunnel with both the light source and the camera located underneath the wind tunnel. The light source is a low pressure sodium lamp SOX35 mounted in a box with a white Plexiglas window to diffuse its light. The camera used was a NIKON D200 mounted on a tripod and operated remotely using NIKON CAPTURE PRO. The angle of the floor and of the lens were measured with an electronic inclinometer. The angle between the glass plate and the camera was calculated from the difference between the floor angle and the angle of the lens. The pictures were recorded in the jpeg format, 'fine' quality with dimensions in pixels of  $3872 \times 2592$ .
- (c) Silicone oil with a viscosity of  $20 \text{ cSt (mm}^2 \text{ s}^{-1})$  is used. The oil viscosity was measured and calibrated as a function of temperature at Ecole Polytechnique Fédérale de Lausanne (EPFL).
- (d) Millimeter paper was placed on the glass plate as a calibration grid and recorded as images to convert the distance between successive fringes from pixels to physical units.

For the present study, we focus on the techniques for determining the fringe spacing and the results are only shown for fringe spacing,  $F_s$ , in pixels. The uncertainty in determining the  $\tau_w$  largely comes from errors in determining the rate of change of fringe spacing, oil viscosity and calibration. By comparing results of fringe spacing in pixels, the discussion of error related to oil viscosity and image calibration is avoided as they depend on a particular experimental setup. Further details of the facility are given by Nickels *et al* [24] and Hutchins and Marusic [25], while Ng *et al* [26] presents previous skin-friction results in the same facility using oil-film interferometry.

#### 5. Analysis examples

Figures 3, 5 and 6 show sample images with the interference pattern from three separate flows with different freestream velocities and ambient conditions. Each image seen on the top is accompanied by a plot showing its grayscale intensity ( $I$ ) profile at a pixel location shown by the solid black line on the image. Typically, the images acquired are in the indexed RGB format and then converted to grayscale intensity. A grayscale profile is preferred as it provides the most contrast between the light and dark fringe patterns. The IMFs,  $C_i$ , obtained by EMD of the intensity profile are shown in plots below each intensity profile. Each figure also shows the amplitude of the Fourier and Hilbert transform plotted against the wavenumber. The dominant wavenumber obtained from a

particular IMF is a function of pixels that on inversion produces the wavelength, which is the fringe spacing, and has units of pixels. One is only required to revert to the time domain when determining the rate of change of the fringe spacing. As here we are interested in determining the mean fringe spacing, the amplitude information of each transform is only used to determine the dominant wavenumber and not scaled to make them equivalent.

Figure 3 shows a ‘clean’ image with the clear fringe pattern reproduced well in the sinusoid wave-like characteristic of the grayscale intensity. One can now use this profile of intensity versus pixels as a signal and determine the wavenumber characteristic of the wave pattern using a signal processing algorithm. It is obvious that this intensity profile is not stationary. The first three IMFs contain the small-scale information associated with the noise in the signal. We find that fringe characteristics of  $I$  are contained in the fourth mode,  $C_4$ . In the algorithm, a correlation between the original signal and the individual IMFs is used to identify the intrinsic mode that contains the fringe characteristics. Compared to  $I$ ,  $C_4$  is symmetric with zero mean. The last mode,  $C_7$ , contains the trend or the traveling mean of the signal,  $I$ . This is a typical outcome of EMD where small-scale information is retained in the first few modes while large scales or low wavenumber characteristics appear in subsequent modes.

Adhering to common practice, the FFT is applied to the mean subtracted intensity profile while the Hilbert transform is applied to the individual IMFs,  $C_i$ . The Hilbert transform when applied to the IMFs generated by EMD proposed by Huang *et al* [13] are known as the Hilbert–Huang transform (HHT). As the HHT gives wavenumber information which varies with time, one can also create a Hilbert marginal spectrum (wavenumber–amplitude–time map). However, for comparison with the FFT and determination of dominant wavenumber, the amplitude versus wavenumber plot shown here will suffice. For each mode,  $n$  number of wavenumbers are determined if the length of  $I$  is  $n$  pixels. As the dominant wavenumber is retained in the fourth mode, it is shown in black in the figure while the amplitude versus wavenumber for the rest of the  $C_i$  are shown in gray for the HHT. The wavenumber obtained from a  $C_i$  at a particular location in  $x$  is associated with its local amplitude and does not necessarily mean that a wave of that wavenumber was the most likely to have persisted through the entire data series. Hence, a median value of the instantaneous wavenumber of the fourth mode is considered as the dominant wavenumber. This wavenumber is shown by a solid black line on the HHT spectra plot. Five ‘x’ marks in the interferometry image for five fringes are placed at a spacing equivalent to the inverse of dominant wavenumber of the HHT spectra (solid black line). It is clear that the instantaneous wavenumber obtained from the HHT is physically relevant and results in a reliable estimate of the fringe spacing. In comparison, the FFT spectrum in figure 3 also shows a sharp peak near the same wavenumber; however, there is a considerable spread of energy at low wavenumber due to the non-stationary behavior of  $I$ . This problem for the FFT can be remedied by removing a traveling mean determined by some method, e.g. a low order polynomial. However, it is not

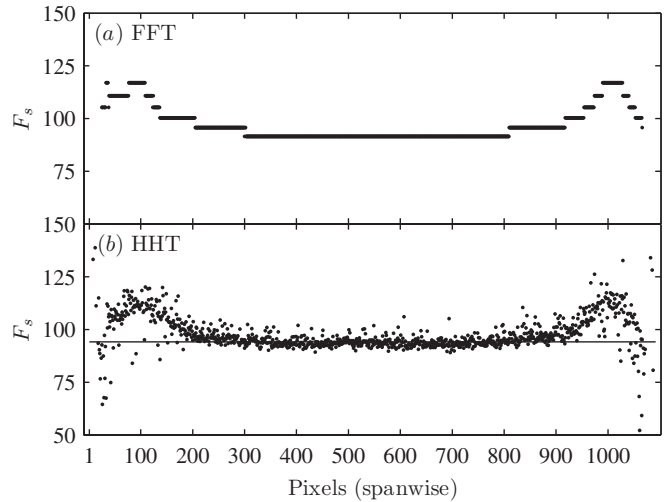


**Figure 4.** Fringe spacing for each pixel line in the spanwise direction obtained for one image.

known *a priori* which functional form will provide the best traveling mean. Such an approach also fails in the presence of sharp discontinuity and low signal-to-noise ratio. For the FFT, only the spectrum above a cutoff wavenumber of  $5/n$  is used to detect a peak to avoid the low wavenumber high energy distribution.

The procedure outlined above is for 1 pixel line in the flow direction. Similarly, the wavenumber is determined for all the pixel lines (parallel to the one shown) in order to obtain a large bin of wavenumbers which are similar. Figure 4 shows fringe spacing obtained for the particular interferogram of figure 3 for all pixel lines using the FFT and HHT as one moves in the spanwise direction (perpendicular to the flow). The three-dimensional effect from the edge and curvature of the oil drop manifests itself in the behavior of fringe spacing in the form of increased  $F_s$  at both ends. The  $F_s$  for the HHT approach is obtained as the median of wavenumbers of the dominant mode (see figure 4(b)). Hence,  $F_{s\text{HHT}}$  behavior has a scatter to it while providing a continuous variation in the spanwise direction. On the other hand, the FFT approach does not detect small changes in the fringe spacing and gives a constant  $F_{s\text{FFT}}$  estimate near the middle of the thin film. The variation in  $F_{s\text{FFT}}$  at either end only appears as ‘step’ changes, which is physically incorrect. Hence, for interferograms where the width of the interference pattern is relatively small, the HHT approach is better posed to identify a region near the center that is devoid of three-dimensional effects. A mean or median of these gives an overall wavenumber and hence the mean fringe spacing that exists throughout the image.

Figure 5 shows a fringe pattern similar to figure 3 but has a large dust particle present near  $x_{\text{pixel}} \approx 1000$ . This results in a sharp discontinuity and drop in the intensity profile, which can lead to dubious results if analyzed by a conventional method. The interference pattern is also seen downstream of the dirt; however, the amplitude of the wave is not uniform unlike the region upstream of the dirt. Again the first three IMFs retain the small-scale information while the fringe pattern appears in  $C_4$ . The fringe pattern downstream is seen in  $C_4$ ; however, it is

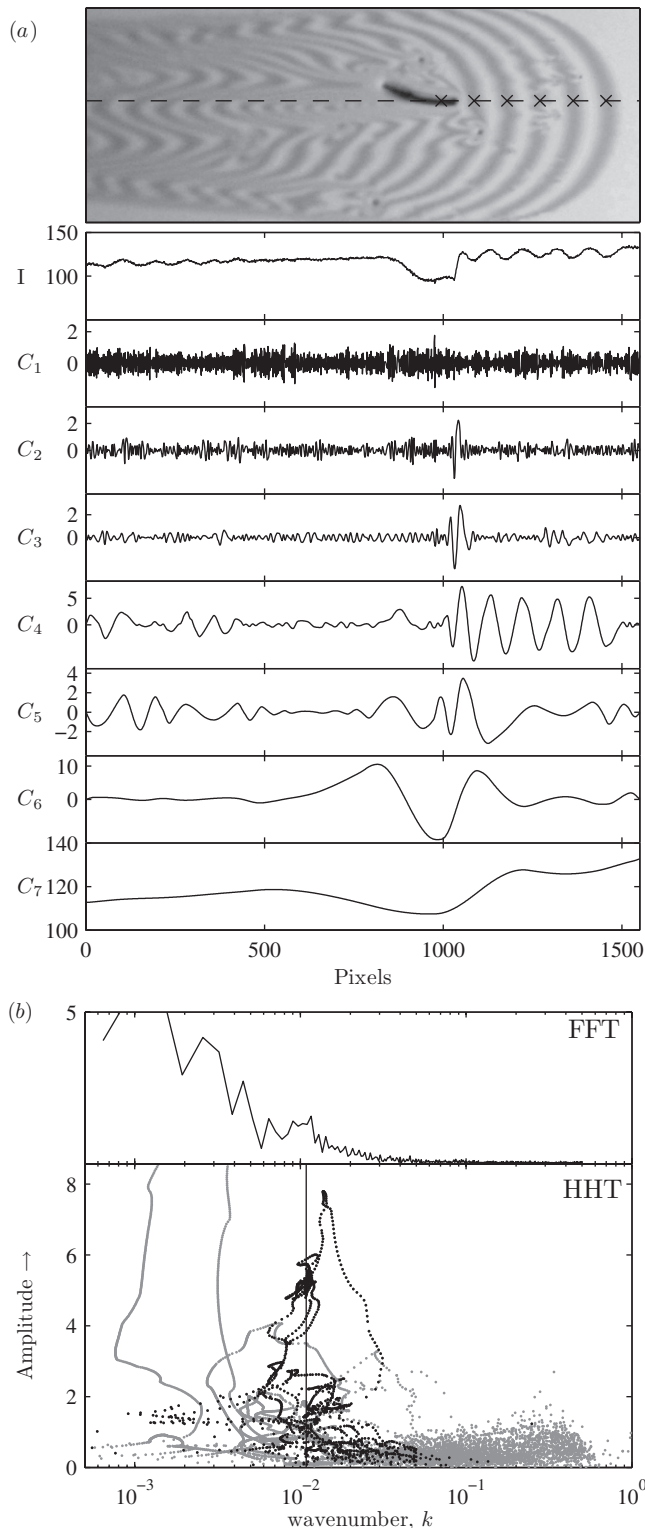


Figure 5. Example 2. See figure 3 for detailed caption.

not uniform as it has been disturbed by the presence of the dirt. The varying intensity is captured in  $C_6$  with a large dip in the profile at the location of the dirt indicating that EMD is useful in finding the moving mean even when sharp discontinuities are present. Applying the HHT on  $C_4$ , the fringe spacing is obtained from the instantaneous wavenumber in HHT spectra,

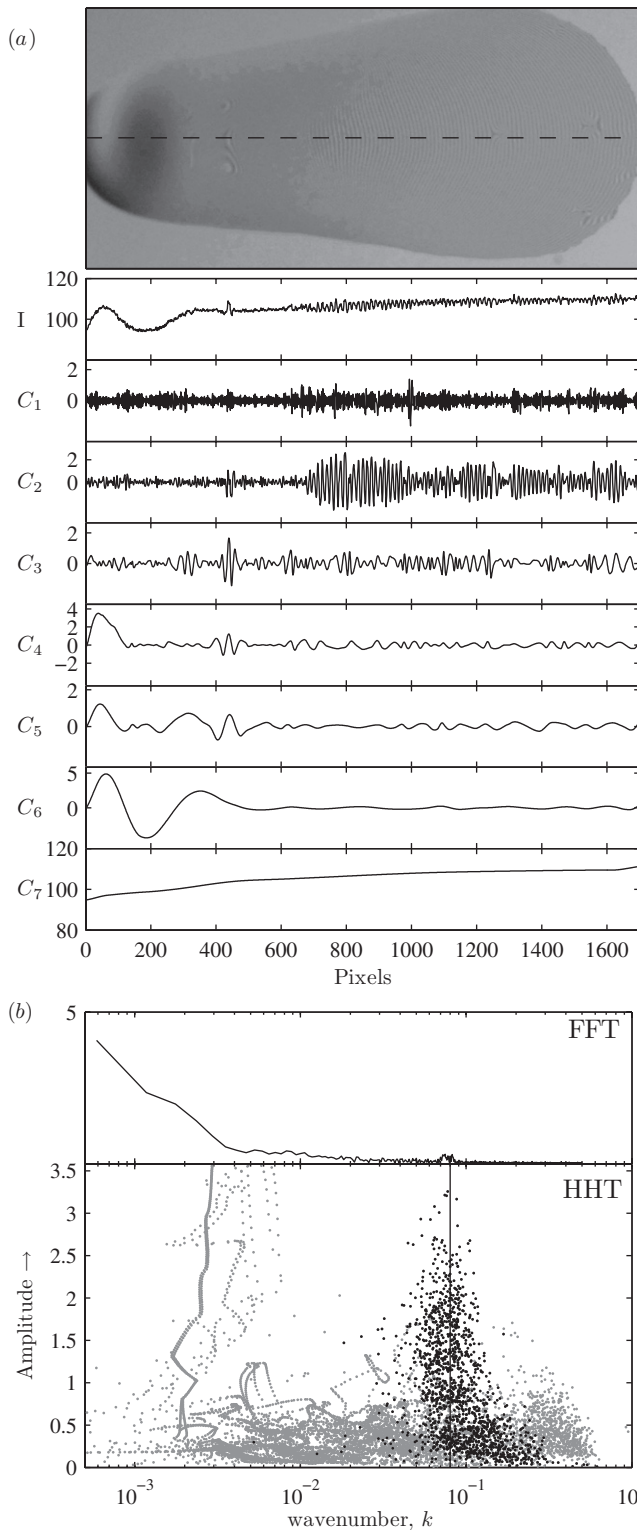
which agrees well with fringes on the grayscale image ('x' marks). The FFT spectrum also shows a peak at the dominant wavenumber but is not as distinct as compared to figure 3. Also, identification of the peak wavenumber from the FFT spectrum is difficult in this case as low wavenumber peaks are amplified due to non-stationarity even if a threshold is used.

Figure 6 shows a clean image but it is acquired relatively early in time as the interference pattern starts developing. The fringe spacing and amplitude of the signal here is quite small compared to the earlier two cases. Also, the width of the oil film rapidly changes to become very narrow downstream. This results in a very short region of signal with the meaningful interference pattern (from  $x_{\text{pixel}} \approx 700$  to  $x_{\text{pixel}} \approx 1600$ ) that can be analyzed at the section chosen to show the intensity profile. Also, an unclean surface can lead to noise in the intensity profile (seen downstream) which can be hard to distinguish if the fringe spacing is small and the contrast is weak. A large dip due to the thick oil that is still developing is seen downstream near  $x_{\text{pixel}} \approx 200$ . For this particular case, the fringe pattern is recovered in the second mode even though it is hard to identify by visual inspection. This is not surprising as the fringe spacing is very small and its period is of the same order as the random noise in the signal, albeit with a much larger amplitude. The HHT spectra for  $C_2$  (shown in black) clearly distinguish the wavenumber associated with fringes appearing with higher amplitude. The noise present in  $C_1$  is at a relatively higher wavenumber with a very low magnitude. Such wavenumber characteristics are impossible to detect in the FFT spectrum, which fails to show a clear peak at a wavenumber associated with the fringe spacing. Again, non-stationarity poses a problem here. If one considers only a part of the signal (e.g. from  $x_{\text{pixel}} \approx 800$  to  $x_{\text{pixel}} \approx 1600$ ) for FFT analysis, then it might be possible to detect the dominant wavenumber. However, choosing a region of analysis for every flow and its many different interference images is not practical. Before proceeding with a discussion of the results and a comparison of the FFT and HHT, some challenges encountered by both the methods will be discussed.

### 5.1. Challenges in implementing the FFT

The FFT, although being a very powerful and widely used tool in signal processing, suffers many limitations in our application of determining the fringe spacing. Here, the demerits are only discussed with respect to the analysis of oil-film interferograms. They are summarized as follows.

- (i) The FFT is only accurate if the signal is linear and stationary. As shown earlier, the intensity profiles from oil-film acquisitions are rarely stationary. The FFT of a non-stationary signal leads to high amplitudes at a relatively low wavenumber, which makes it difficult to distinguish the physically relevant wavelength associated with fringe spacing.
- (ii) A moving or traveling mean can be subtracted to remove the non-stationarity from the signal. However, this approach has to be tailored for the varying quality of the images. Specific to interferograms, the non-stationary



**Figure 6.** Example 3. See figure 3 for detailed caption.

behavior depends on the ambient light conditions and hence, for different experimental setups different methods for extracting the traveling mean might be needed. As shown in figure 5, such an approach is still not helpful in treating nonlinearity or discontinuities in the signal.

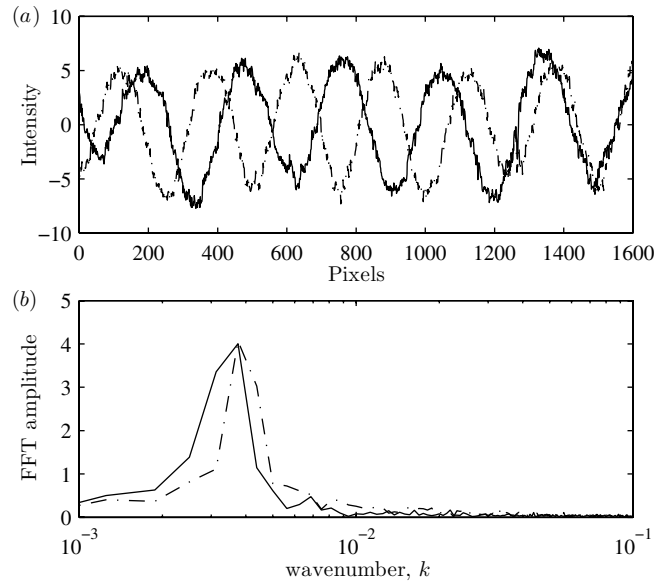


**Figure 7.** (a) Two intensity profiles along a pixel line after removing traveling mean from a set of acquisitions 80 s apart in the same flow. (b) Amplitude of the FFT on the profiles.

- (iii) For very small fringe spacings, the FFT provides no qualitative distinction between the signal noise and the wave itself. For images with weak contrast, this would lead to a relatively flat spectrum making it difficult to locate the peak.
- (iv) The FFT for signals of length  $n$  can only resolve  $n/2 + 1$  frequencies with each frequency cell being  $2/n$  wide. For the short sample size of a wave with a relatively large period, the estimate of dominant frequency is often inaccurate. This limitation is more prominently encountered in interferograms with a small number of fringes. Figure 7 shows intensity profiles from two images acquired from the same flow. The dash-dotted profile is from an image acquired at an earlier time while the solid profile is from an image acquired after 80 s. It is clearly seen that the distance between two subsequent zero crossings for the solid line (five fringes) is higher than the dash-dotted one (six fringes) indicating larger fringe spacing. This is further evident by considering that a sinusoidal pattern fitted to the intensity profiles will give six crests for the dash-dotted line while five crests for the solid line. However, the FFT spectrum for both the profiles peaks at the same wavenumber because the actual wavenumbers, say  $k_1$  and  $k_2$ , correspond to the same frequency cell. This resolution limitation is quite common when the change in fringe spacing of two consecutive image acquisitions is smaller than  $2/n$ . The wavenumbers in the discrete Fourier transform are linearly spaced and hence the inverse of these would have a nonlinear variation in physical or space coordinates. On the other hand, the fringe spacing for oil-film interferograms changes linearly with time and hence will require large sample lengths,  $n$ , to resolve small changes in the low wavenumber (high  $F_s$ ) characteristics. Auto-correlation methods can help in

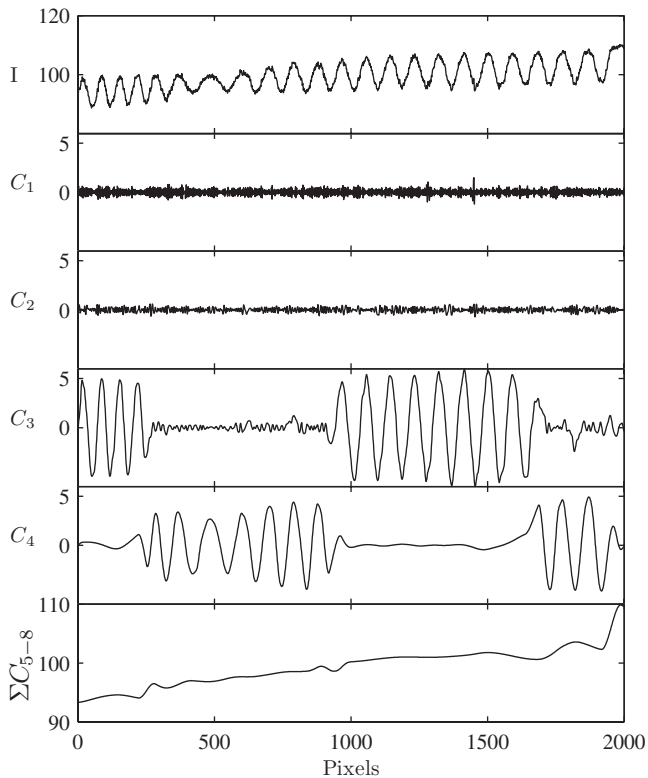


**Figure 8.** IMFs for an intensity profile showing mode mixing between  $C_3$  and  $C_4$ .

overcoming this limitation if the curvature of fringes is not too high.

### 5.2. Challenges in implementing the HHT

The main challenges encountered in implementing the HHT are summarized as follows.

- (i) When generating the envelopes required by EMD, the treatment of end conditions requires special attention. Typically, cubic splines are fitted to the local maxima and minima in order to generate the upper and lower envelopes. However, fitting a cubic spline to the data can be problematic at the ends because large swings can be generated [13]. These end swings can then propagate inward, generating new artificial extremum and eventually generating spurious intrinsic modes of low wavenumber. To limit these, whilst maintaining low computational expense, we have chosen to add a sine wave at both the ends. The amplitude of this wave is characterized by the first two extrema at each end. This approach works with the assumption that the imaginary signal preceding and following the signal has the same wave characteristics.
- (ii) Another difficulty that is typically encountered is a phenomena called ‘mode mixing’ [14]. Figure 8 shows IMFs for an intensity profile which also has random noise on the fringe pattern. After applying EMD, it is seen that the wave characteristic associated with the fringe pattern is present in both  $C_3$  and  $C_4$  instead of being a continuous occurrence in either one of them. As the

same component of wavenumber is present in two modes, one can say that the component of  $C_4$  is ‘mixed’ with  $C_3$ . Mode mixing occurs due to the presence of ‘riding waves’, which are small wavelength and amplitude fluctuations residing on top of larger waves. Mode mixing can be a common occurrence in interferogram analysis as the surface conditions are not ideal and small amplitude noise is always present on the fringe pattern. Riding waves will cause the envelope mean to travel along the signal instead of its line of symmetry. Such mixing of modes can be problematic when determining the dominant wavenumber as the amplitude versus wavenumber characteristic of  $C_3$  will be quite wide (both low and high wavenumbers present). Also, the peak amplitude for both  $C_3$  and  $C_4$  will be attenuated. In the present study, the covariance between the original signal and the individual IMFs is used to determine which IMF contains the information of the dominant wavenumber. Covariance being the measure of how much two variables change together is a direct means of statistically relating the original signal and IMF with the fringe pattern. If mode mixing occurs, such a statistical determination might fail because of the lack of correlation for both the modes with the original signal.

One approach to tackle mode mixing is to evaluate the distance between two consecutive zero crossings. For  $C_3$  in figure 8, a histogram of the period between zero crossings will be populated for both small and large periods. A upper limit criterion can be implemented, which limits the period size allowed in a particular mode. Any wave with a higher period is then replaced by the local envelope mean so that it is ‘forced’ to go to the next IMF, which by nature of EMD should contain the large-scale information. Figure 9 shows this implementation where the large amplitude and period waves in  $C_3$  are replaced by the local mean and they now appear in  $C_4$ . The IMF  $C_4$  can now provide the dominant wavenumber estimate more accurately. A low pass filter on the original signal to remove the small-scale disturbances and riding waves can also be used. Mode mixing rarely occurs for a filtered signal. However, because the fringes spacing typically changes from very small to quite large, such a filter should only be implemented after a good estimate of accuracy and errors of the overall procedure are known.

In the present study, we have not treated the data for mode mixing by either of the above methods. The reason is to avoid any sort of subjectivity to the analysis. The aim of this paper is to use the HHT as a tool which can be adopted by readers for similar studies. Hence, the strengths and weaknesses of the HHT applied to interferograms are presented here by keeping the procedure in an elementary form. A user can further make improvements to the techniques by customizing it to their own applications if required.

## 6. Results and discussion

Figures 10 and 11 plot fringe spacing versus time for two zero pressure gradient boundary layer flow experiments in the Melbourne wind tunnel. The fringe pattern seen in the last image acquired is shown on the top. It should be noted

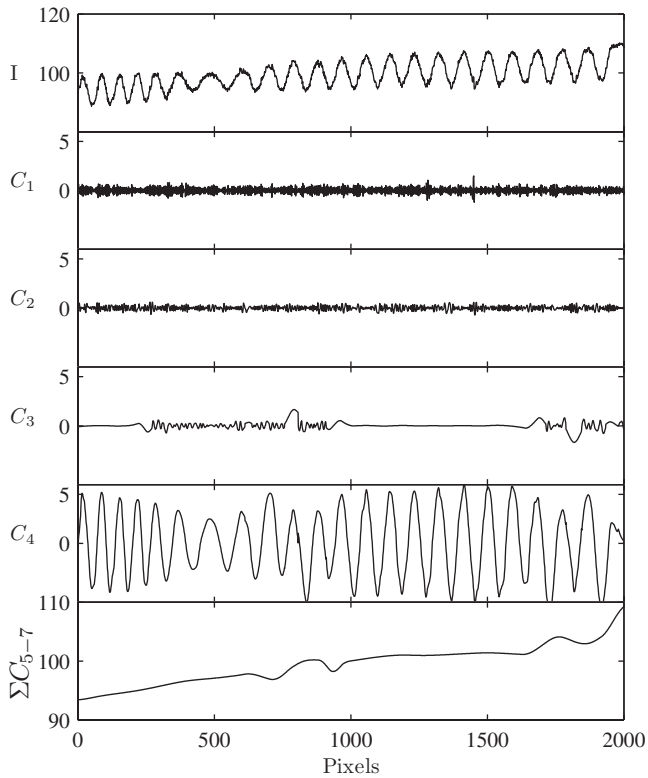


**Figure 9.** IMFs for the same intensity profile as in figure 8 after treating for mode mixing. The histogram of zero crossings is used to exclude large period waves in  $C_3$ . Note that  $C_1$  and  $C_2$  are the same as in figure 8.

that in a particular experiment the images are captured at a certain time interval which depends on the oil viscosity and freestream velocity. In figures 10 and 11, the abscissa is the image number, which can be conveniently converted to time by multiplying the time interval between consecutive images. In these experiments, multiple drops of oil were used side by side. These are denoted by ‘a’, ‘b’ and ‘c’ on the image. The fringe spacing for a particular image number is the ensemble mean obtained from wavenumbers estimated from each streamwise pixel line using the HHT and FFT. As the fringe spacing varies linearly with time, a least-squares fit gives the slope,  $dF_s/dt$  (pixels  $s^{-1}$ ). A calibration image for each setup makes it possible to obtain  $dF_s/dt$  in  $m s^{-1}$ , which can be substituted in equation (1) for  $\Delta x/\Delta t$ . The numerical values of slope obtained for each fringe pattern from the HHT and FFT are listed on the plot along with their percentage difference. Also, a parameter  $F_\epsilon$  is defined as

$$F_\epsilon = \sqrt{\frac{1}{N} \sum (F_{s\text{HHT}} - F_{s\text{FFT}})^2}, \quad (12)$$

where  $N$  is the total number of images fitted to estimate the slope and  $F_{s\text{HHT}}$  and  $F_{s\text{FFT}}$  are the fringe spacing estimated using the HHT and FFT, respectively. Here,  $F_\epsilon$  serves as a statistical measure of difference between the HHT and FFT estimates of fringe spacing in pixels.

The interference pattern in figure 10 is clean and devoid of any dust or contamination. It is not surprising that the slopes

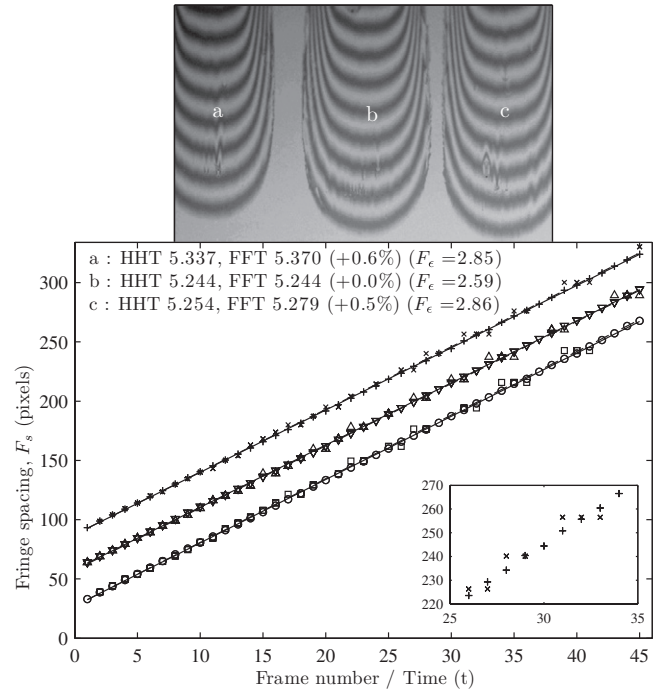


**Figure 10.** Fringe spacing,  $F_s$  versus image number (time) for ZPG flow in the Melbourne tunnel at  $U_\infty = 20 \text{ m s}^{-1}$  at station 3 ( $x \approx 21\text{m}$ ). Symbols ‘o’, ‘ $\nabla$ ’ and ‘+’ represent  $F_{s\text{HHT}}$  for oil drops ‘a’, ‘b’ and ‘c’, respectively. Symbols ‘ $\square$ ’, ‘ $\triangle$ ’ and ‘ $\times$ ’ represent  $F_{s\text{FFT}}$  for oil drops ‘a’, ‘b’ and ‘c’, respectively. Solid lines are linear least-squares fits. Note the shift of 30 units between data points for ‘a’, ‘b’ and ‘c’. The inset shows magnified comparison for the oil film ‘c’ clearly showing the step change in  $F_{s\text{FFT}}$ . Approximately 2000 pixels in the streamwise direction are used for EMD.

evaluated for the HHT and FFT agree very well with each other. Also,  $F_\epsilon \approx 3$  suggests that the fringe spacing obtained by these two methods would at most disagree by 9 pixels (three standard deviations), which is quite small compared to  $F_s \sim 250$  pixels for the final images. However, it should be noted that such a good agreement is only obtained by discarding  $F_s$  estimates by the FFT, which suffer from the problem of wavenumber resolution. It can be seen that  $F_{s\text{FFT}}$  toward the end of the acquisition does not change for a certain consecutive set of images and then suddenly jumps to a higher value. This is due to the jump of dominant wavenumber from one wavenumber cell to another as discussed earlier in section 5.1. The data points which have the same  $F_{s\text{FFT}}$  as the previous or next image are not used to determine the slope. It is clear that in the absence of the HHT, the FFT would not provide an accurate estimate of  $F_s$  for the latter part of the acquisitions. The instantaneous wavenumber of the Hilbert transform does not suffer from a limitation of wavenumber range and only depends on the accuracy of determining  $d\omega/dt$  (equation (6)). Hence, even when the fringe spacing is large (or only a few fringes are seen in the interrogation region), the HHT can provide an accurate estimate of the wavenumber from the IMFs. This is clearly evident by the linear behavior of  $F_{s\text{HHT}}$  all throughout in contrast to the ‘step’ behavior of  $F_{s\text{FFT}}$  toward the end of the acquisition.

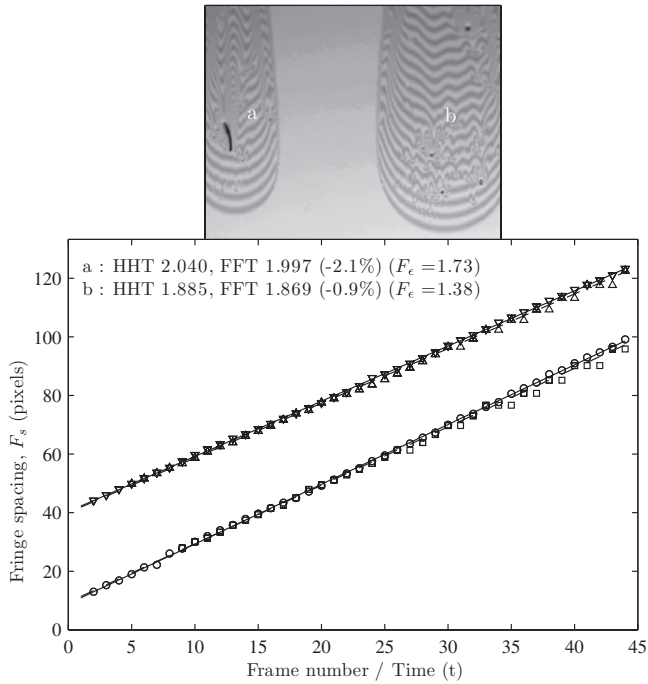


**Figure 11.** Fringe spacing,  $F_s$ , versus image number (time) for ZPG flow in the Melbourne tunnel at  $U_\infty = 12 \text{ m s}^{-1}$  at station 2 ( $x \approx 13 \text{ m}$ ). Symbols ‘ $\circ$ ’ and ‘ $\nabla$ ’ represent  $F_{s\text{HHT}}$  for oil drops ‘a’ and ‘b’, respectively. Symbols ‘ $\square$ ’ and ‘ $\Delta$ ’ represent  $F_{s\text{FFT}}$  for oil drops ‘a’ and ‘b’, respectively. Solid lines are linear least-squares fits.

Figure 11 shows a similar plot as figure 10 for interferometry at different streamwise locations and freestream velocities. Compared to figure 10, freestream velocity in this case is lower, resulting in the maximum fringe spacing being near 100 pixels (compared to  $\sim 250$  in figure 10) after the same amount of time has elapsed. The problem of wavenumber resolution is also present in this case. However, this particular case has been chosen because of the presence of a distinctly large dust particle on the left oil film ‘a’ and a patch of surface contamination on oil film ‘b’. This results in a very poor interference pattern that would be discarded if analyzed by any conventional approach like the  $x-t$  diagram of figure 2. Even selecting a clear region of the fringe pattern manually would be difficult as it would have a only small region with a clear interference pattern. However, it is found that the HHT approach works consistently well even in this case resulting in linear behavior of  $F_{s\text{HHT}}$ . On the other hand,  $F_{s\text{FFT}}$  shows considerable scatter along its linear behavior resulting in a 2.1% difference in the estimated slope for oil film ‘b’. Such a difference is significant as the expected accuracy of oil-film interferometry is to be typically bound within  $\pm 1.5\%$ . The estimate of wall shear stress can only be as accurate as the accuracy of the estimated slope ( $\Delta x/\Delta t$ ) if the other parameters are accurately known. In contrast, even though the inference pattern in ‘b’ is not clear, we see that the percentage difference between  $F_{s\text{HHT}}$  and  $F_{s\text{FFT}}$  is relatively small. This is due to the overall larger width of the oil film in ‘b’, which initially contained a larger volume of oil drop to start with. A wider fringe pattern gives more samples of wavenumber that are estimated from pixel lines in the flow direction and

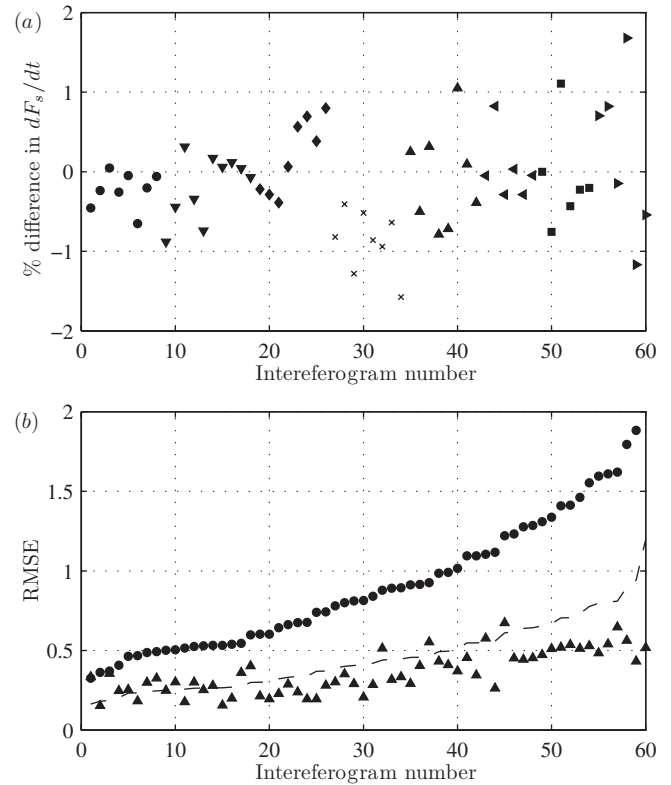


**Figure 12.** (a) Percentage difference for  $dF_s/dt$  between the FFT and HHT approach for all interferograms (each data point corresponds to a single oil drop). Symbols denote: ‘ $\bullet$ ’, ‘ $\nabla$ ’ and ‘ $\blacklozenge$ ’ for  $U_\infty = 12, 17$  and  $21 \text{ m s}^{-1}$ , respectively, at station 1; ‘ $\times$ ’ for  $U_\infty = 12 \text{ m s}^{-1}$  at station 2; ‘ $\blacktriangle$ ’, ‘ $\blacktriangleleft$ ’, ‘ $\blacksquare$ ’ and ‘ $\blacktriangleright$ ’ for  $U_\infty = 10, 15, 20$  and  $25 \text{ m s}^{-1}$ , respectively, at station 3. (b) Root-mean-square error of linear fit to the  $F_s$  versus  $t$  data for the FFT and HHT approach. ‘ $\bullet$ ’, RMSE for fits to  $F_{s\text{FFT}}$  versus  $t$ ; ‘ $\blacktriangle$ ’, RMSE for fits to  $F_{s\text{HHT}}$  versus  $t$ . Data points are arranged in increasing order of RMSE from the FFT approach (‘ $\bullet$ ’) and dashed line is half its value.

subsequently averaged. A small oil drop will form a narrow fringe pattern with high curvature and the three-dimensional effects can lead to an inaccurate fringe spacing estimate.

Finally, figure 12 shows two comparisons for the FFT and HHT approach to find  $dF_s/dt$ . First, the percentage difference between  $dF_s/dt$  obtained using the FFT and HHT is shown in figure 12(a) for all 60 cases of oil-film interferograms available from the experiments for the zero pressure gradient boundary layer. These include measurement at different stations with different freestream velocities and also the multiple acquisitions made for similar flow conditions. It is found that the typical difference between the FFT and HHT approaches for estimated  $dF_s/dt$  is within  $\pm 1\%$ , which is about the same as the expected error in determining  $\tau_w$  from oil-film interferometry. This emphasizes the need for accurately determining  $dF_s/dt$ , an error in which linearly contributes to the error of  $\tau_w$  (equation (1)). As the thickness of thin film changes linearly with time, we compare the linearity of  $F_s$  versus  $t$  obtained using FFT and HHT approaches. This is achieved by comparing the root-mean-square error (RMSE) of linear fits to  $F_s$  versus  $t$  as shown in figure 12(b). A small

RMSE would indicate that the estimated development of  $F_s$  versus  $t$  is in close agreement to the physical linear behavior. It is clear from figure 12(b) that the HHT approach considerably improves the accuracy of estimating the linear variation of  $F_s$  versus  $t$  with RMSE less than half of RMSE for the FFT approach. Hence, figure 12(b) compliments figure 12(a) to indicate that the error involved in determining  $dF_s/dt$  can be reduced by at least 50% by adopting the HHT approach.

## 7. Conclusions

In the present study, a large database of oil-film interferometry acquisitions is analyzed using two approaches: FFT and HHT. While FFT methods are conventionally used in determining the fringe spacing, they often require some user input in the form of region selection, removal of non-stationarity and sometimes peak identification. Even when such care is implemented in the analysis, it still falls short of being accurate for images that have dust and contamination. The Hilbert–Huang transform on the other hand does not suffer from the limitations of the FFT listed in section 5.1, and although, it poses its own challenges in the form of mode mixing and end effects, these are not found to be limiting for application. Both mode mixing and end effects can be treated by adopting the EMD algorithms to suit the characteristics of the signal being measured, though the higher computational cost associated with EMD (and sifting) is unavoidable. On the other hand, the FFT is simple to implement and computationally fast algorithms are readily available due to its popularity. Overall, key benefits of using the HHT over the FFT as a procedure for extracting fringe spacing can be explicitly listed as follows.

- (i) The HHT does not suffer from the problem of inadequate wavenumber resolution. The instantaneous wavenumber only depends on the shape of the IMF and hence the HHT even on a short signal length can provide significant information.
- (ii) EMD isolates the fringe characteristics to a particular IMF while the noise and low wavenumber characteristics are typically in other modes. Hence, wavenumber identification is relatively easier as compared to the FFT spectrum.
- (iii) The HHT can be applied to non-stationary and nonlinear data. It can also handle interferograms with dirt and surface contamination, which can have sharp discontinuities and uneven wave patterns in the intensity profile.

It is advisable to have a sufficiently high number of fringes in the images acquired to use the Fourier transform for extracting fringe spacing. Typically, one has to balance between three important parameters in the experiment: the freestream velocity, the viscosity of oil and the time available for the acquisition of interferograms. This requires choosing different oil viscosities for different freestream velocities for best result. At high freestream velocities, the fringe spacing can be quite large and the oil film is closest to the thin-film approximation. A high oil viscosity is preferred in such instances. On the other hand, short acquisition times would

require relatively low viscosity of oil so that enough linear change in fringe spacing is observed to determine the slope. Such an adaptation of parameters is not straightforward and tedious. The approach of using the HHT eliminates such tweaking of parameters as it is able to extract fringe spacing even from short signal length or interferograms with few fringes visible. Also, it provides a good linear estimate of  $F_s$  even over short acquisition times to reliably estimate the slope,  $dF_s/dt$  (see figure 10).

It should be noted that the HHT approach does require some user adaptation in the form of selecting the right sifting stop criteria, treatment of end effects, treatment of mode mixing and extracting a single value of wavenumber from a time-varying wavenumber distribution. However, these only affect the quantitative results presented in this paper while the inherent advantages over Fourier methods remain intact. The advantages and applicability of the HHT makes it a very robust technique to determine fringe spacing. As highlighted in the previous section, the HHT approach determines  $dF_s/dt$  more accurately than the FFT, while their results can differ by few a percentage. Hence, using the HHT as a primary tool in analysis of interferograms will only improve the already most accurate technique of oil-film interferometry for wall shear stress measurements.

## Acknowledgments

The authors would like to thank Dr J D Rüedi of the University of Bologna for providing some of the interferograms that were acquired as a part of measurements for International Collaboration on Experiments in Turbulence (ICET), and for the calibration of the silicone oil viscosity. This work was supported by funding from the Australian Research Council.

## References

- [1] Tropea C, Yarin A L and Foss J F (eds) 2007 *Springer Handbook of Experimental Fluid Mechanics* (Berlin: Springer)
- [2] Fernholz H H, Janke G, Schober M, Wagner P M and Warnack D 1996 New developments and applications of skin-friction measuring techniques *Meas. Sci. Technol.* **7** 1396–409
- [3] Naughton J W and Sheplak M 2002 Modern developments in shear-stress measurement *Prog. Aerosp. Sci.* **38** 515–70
- [4] Rüedi J D, Nagib H, Österlund J and Monkewitz P A 2003 Evaluation of three techniques for wall-shear measurements in three-dimensional flows *Exp. Fluids* **35** 389–96
- [5] Heuer W D C and Marusic I 2005 Turbulence wall-shear stress sensor for the atmospheric surface layer *Meas. Sci. Technol.* **16** 1644–9
- [6] Clauser F H 1954 Turbulent boundary layers in adverse pressure gradients *J. Aeronaut. Sci.* **21** 91–108
- [7] Clauser F H 1956 The turbulent boundary layer *Adv. Appl. Mech.* **4** 1–51
- [8] Preston J H 1954 Determination of turbulent skin friction by means of pitot tubes *J. R. Aeronaut. Soc.* **58** 109–21
- [9] Patel V C 1965 Calibration of the Preston tube and limitations on its use in pressure gradients *J. Fluid Mech.* **23** 185–208
- [10] Naughton J W, Robinson J and Durgesh V 2003 Oil-film interferometry measurement of skin friction—analysis and description of Matlab program *Proc. 20th Int. Congress on*

- Instrumentation in Aerospace Simulation Facilities* pp 169–178
- [11] Zilliac G G 1996 Further developments of the fringe imaging skin friction technique *NASA Technical Memorandum 110425*
- [12] Decker R K, Naughton J W and Jafari F 2000 Automatic fringe detection for oil film interferometric skin friction measurement *9th Int. Symp. on Flow Visualisation* ed I Grant and G M Carlomagno, paper 368
- [13] Huang N E, Zheng S, Long S R, Wu M C, Shih H H, Zheng Q, Yen N, Tung C C and Liu H H 1998 The empirical mode decomposition and the Hilbert spectrum for non-linear and non-stationary time series analysis *Proc. R. Soc. A* **454** 903–95
- [14] Huang N E, Zheng S and Long S R 1999 A new view of nonlinear water waves: the Hilbert spectrum *Annu. Rev. Fluid Mech.* **31** 417–57
- [15] Tanner L H and Blows L G 1976 A study of the motion of oil films on surfaces in air flow, with application to the measurement of skin friction *J. Phys. E: Sci. Instrum.* **9** 194–202
- [16] Squire L C 1961 The motion of a thin oil sheet under the steady boundary layer on a body *J. Fluid Mech.* **11** 161–79
- [17] Tanner L H 1977 A comparison of the viscosity balance and Preston tube methods of skin friction measurement *J. Phys. E: Sci. Instrum.* **10** 627–32
- [18] Tanner L H 1977 A skin friction meter, using the viscosity balance principle, suitable for use with flat or curved metal surfaces (based on thickness measurement) *J. Phys. E: Sci. Instrum.* **10** 278–84
- [19] Tanner L H and Kulkarni V G 1976 The viscosity balance method of skin friction measurement: further developments including applications to three-dimensional flow *J. Phys. E: Sci. Instrum.* **9** 1114–21
- [20] Monson D J 1983 A nonintrusive laser interferometer method for measurement of skin friction *Exp. Fluids* **1** 15–22
- [21] Monson D J and Higuchi H 1981 Skin friction measurements by a dual-laser-beam interferometer technique *AIAA J.* **19** 739–44
- [22] Schülein E 2003 Optical skin friction measurements in the short-duration Ludwig tube facility *Proc. 20th Int. Congress on Instrumentation in Aerospace Simulation Facilities* pp 157–68
- [23] Bendat J S and Piersol A G 2000 *Random Data: Analysis and Measurement Procedures* 3rd edn (New York: Wiley)
- [24] Nickels T B, Marusic I, Hafez S M, Hutchins N and Chong M S 2007 Some predictions of the attached eddy model for a high Reynolds number boundary layer *Phil. Trans. R. Soc. London A* **365** 807–22
- [25] Hutchins N and Marusic I 2007 Evidence of very long meandering features in the logarithmic region of turbulent boundary layers *J. Fluid Mech.* **579** 1–28
- [26] Ng H C H, Marusic I, Monty J P, Hutchins N and Chong M S 2007 Oil film interferometry in high Reynolds number turbulent boundary layers *Proc. 16th Australasian Fluid Mechanics Conf.* pp 807–14